

Multiwavelength observations of the blazar BL Lacertae: a new fast TeV γ -ray flare

This work was made openly accessible by BU Faculty. Please [share](#) how this access benefits you. Your story matters.

Version	
Citation (published version):	Q. Feng, for the VERITAS Collaboration, S. G. Jorstad, A. P. Marscher, M. L. Lister, Y. Y. Kovalev, A. B. Pushkarev, T. Savolainen, I. Agudo, S. N. Molina, J. L. Gomez, V. M. Larionov, G. A. Borman, A. A. Mokrushina, P. S. Smith. "Multiwavelength observations of the blazar BL Lacertae: a new fast TeV γ -ray flare." Proceedings of the 35th International Cosmic Ray Conference (ICRC 2017), Busan (South Korea).

<https://hdl.handle.net/2144/25748>

Boston University

MULTIWAVELENGTH OBSERVATIONS OF THE BLAZAR BL LACERTAE: A NEW FAST TEV GAMMA-RAY FLARE

A. U. ABEYSEKARA,¹ W. BENBOW,² R. BIRD,³ R. BROSE,^{4,5} M. BUCHOVECKY,³ V. BUGAEV,⁶
M. P. CONNOLLY,⁷ W. CUI,^{8,9} M. K. DANIEL,² A. FALCONE,¹⁰ Q. FENG,^{11,12} L. FORTSON,¹³
I. GUNAWARDHANA,¹ M. HÜTTEN,⁵ D. HANNA,¹¹ O. HERVET,¹⁴ J. HOLDER,¹⁵ G. HUGHES,²
T. B. HUMENSKY,¹² C. A. JOHNSON,¹⁴ P. KAARET,¹⁶ P. KAR,¹ M. J. LANG,⁷ M. KERTZMAN,¹⁷
F. KRENNRICH,¹⁸ M. J. LANG,⁷ T. T.Y. LIN,¹¹ P. MORIARTY,⁷ R. MUKHERJEE,¹⁹ S. O'BRIEN,²⁰
R. A. ONG,³ N. PARK,²¹ A. PETRASHYK,¹² M. POHL,^{4,5} E. PUESCHEL,⁵ J. QUINN,²⁰ K. RAGAN,¹¹
P. T. REYNOLDS,²² G. T. RICHARDS,²³ E. ROACHE,² C. RULTEN,¹³ I. SADEH,⁵ G. H. SEMBROSKI,⁸
S. P. WAKELY,²¹ R. M. WELLS,¹⁸ P. WILCOX,¹⁶ AND D. A. WILLIAMS¹⁴

(THE VERITAS COLLABORATION)

S. G. JORSTAD,^{24,25} A. P. MARSCHER,²⁴ M. L. LISTER,²⁶ Y. Y. KOVALEV,^{27,28,29}
A. B. PUSHKAREV,^{30,27} T. SAVOLAINEN,^{31,32,29} I. AGUDO,³² S. N. MOLINA,³³ J. L. GÓMEZ,³³
V. M. LARIONOV,²⁵ G. A. BORMAN,³⁴ A. A. MOKRUSHINA,²⁵ M. TORNIKOSKI,³¹
A. LÄHTEENMÄKI,^{31,32,35} W. CHAMANI,^{31,32} S. ENESTAM,^{31,32} S. KIEHLMANN,³⁶ T. HOVATTA,³⁷
P. S. SMITH,³⁸ AND P. PONTRELLI¹⁴

¹*Department of Physics and Astronomy, University of Utah, Salt Lake City, UT 84112, USA*

²*Fred Lawrence Whipple Observatory, Harvard-Smithsonian Center for Astrophysics, Amado, AZ 85645, USA*

³*Department of Physics and Astronomy, University of California, Los Angeles, CA 90095, USA*

⁴*Institute of Physics and Astronomy, University of Potsdam, 14476 Potsdam-Golm, Germany*

⁵*DESY, Platanenallee 6, 15738 Zeuthen, Germany*

⁶*Department of Physics, Washington University, St. Louis, MO 63130, USA*

⁷*School of Physics, National University of Ireland Galway, University Road, Galway, Ireland*

⁸*Department of Physics and Astronomy, Purdue University, West Lafayette, IN 47907, USA*

⁹*Department of Physics and Center for Astrophysics, Tsinghua University, Beijing 100084, China.*

¹⁰*Department of Astronomy and Astrophysics, 525 Davey Lab, Pennsylvania State University, University Park, PA 16802, USA*

¹¹*Physics Department, McGill University, Montreal, QC H3A 2T8, Canada*

¹²*Physics Department, Columbia University, New York, NY 10027, USA*

¹³*School of Physics and Astronomy, University of Minnesota, Minneapolis, MN 55455, USA*

¹⁴*Santa Cruz Institute for Particle Physics and Department of Physics, University of California, Santa Cruz, CA 95064, USA*

¹⁵*Department of Physics and Astronomy and the Bartol Research Institute, University of Delaware, Newark, DE 19716, USA*

¹⁶*Department of Physics and Astronomy, University of Iowa, Van Allen Hall, Iowa City, IA 52242, USA*

¹⁷*Department of Physics and Astronomy, DePauw University, Greencastle, IN 46135-0037, USA*

¹⁸*Department of Physics and Astronomy, Iowa State University, Ames, IA 50011, USA*

¹⁹*Department of Physics and Astronomy, Barnard College, Columbia University, NY 10027, USA*

²⁰*School of Physics, University College Dublin, Belfield, Dublin 4, Ireland*

²¹*Enrico Fermi Institute, University of Chicago, Chicago, IL 60637, USA*

²²*Department of Physical Sciences, Cork Institute of Technology, Bishopstown, Cork, Ireland*

²³*School of Physics and Center for Relativistic Astrophysics, Georgia Institute of Technology, 837 State Street NW, Atlanta, GA 30332-0430*

²⁴*Institute for Astrophysical Research, Boston University, 725 Commonwealth Avenue, Boston, MA 02215, USA*

²⁵*Astronomical Institute, St.Petersburg State University, Universitetskij Pr. 28, Petrodvorets, 198504 St.Petersburg, Russia*

²⁶*Purdue University, 525 Northwestern Avenue, West Lafayette, IN 47907, USA*

²⁷*Astro Space Center of Lebedev Physical Institute, Profsoyuznaya 84/32, 117997 Moscow, Russia*

²⁸*Moscow Institute of Physics and Technology, Dolgoprudny, Institutskiy per., 9, Moscow region, 141700, Russia*

²⁹*Max-Planck-Institut für Radioastronomie, Auf dem Hügel 69, 53121 Bonn, Germany*

³⁰*Crimean Astrophysical Observatory, 98409 Nauchny, Crimea, Russia*

³¹*Aalto University Metsähovi Radio Observatory, Metsähovintie 114, FI-02540 Kylmälä, Finland*

³²*Aalto University Department of Electronics and Nanoengineering, PL 15500, FI-00076 Aalto, Finland*

³³*Instituto de Astrofísica de Andalucía (CSIC), Apartado 3004, E-18080 Granada, Spain*

³⁴*Crimean Astrophysical Observatory, 98409 Nauchny, Crimea, Russia*

³⁵*Tartu Observatory Observatooriumi 161602 Tõravere, Estonia*

³⁶*Owens Valley Radio Observatory, California Institute of Technology, Pasadena, CA 91125, USA*

³⁷*Tuorla Observatory, Department of Physics and Astronomy, University of Turku, Väisäläntie 20, 21500 Kaarina, Finland*

³⁸*Steward Observatory, University of Arizona, Tucson, AZ 85716, USA*

ABSTRACT

Combined with very-long-baseline radio interferometry measurements, the observations of fast TeV gamma-ray flares probe the structure and emission mechanism of blazar jets. However, only a handful of such flares have been detected to date, and only within the last few years have these flares been observed from lower-frequency-peaked BL Lac objects and flat-spectrum radio quasars. We report on a fast TeV gamma-ray flare from BL Lacertae observed by VERITAS, with a rise time of ~ 2.3 hr and a decay time of ~ 36 min. The peak flux above 200 GeV measured with a 4-minute-binned light curve is $(4.2 \pm 0.6) \times 10^{-6}$ photon $\text{m}^{-2} \text{s}^{-1}$, or $\sim 180\%$ of the flux which is observed from the Crab Nebula above the same energy threshold. Variability in GeV gamma-ray, X-ray, and optical flux, as well as in optical and radio polarization, was observed around the time of the TeV gamma-ray flare. Additionally, a possible superluminal knot was identified in VLBA observations at 43 GHz, potentially passing the radio core of the jet around the time of the gamma-ray flare. We discuss the constraints on the size, Lorentz factor, and location of the emitting region of the flare, and the interpretations with several theoretical models which invoke relativistic plasma passing stationary shocks.

Keywords: galaxies: active – BL Lacertae objects: individual (BL Lacertae = VER J2202+422)

1. INTRODUCTION

BL Lac objects belong to a subclass of radio-loud active galactic nuclei (AGNs), known as blazars. They are characterized by featureless optical spectra, non-thermal broadband spectra, and rapid variability, which jointly suggest that their emission originates in relativistic jets closely aligned to our line of sight (e.g., [Schlick-eiser 1996](#)).

Some TeV blazars exhibit fast gamma-ray variability, the timescale of which can be as short as a few minutes at very high energies (100 GeV $\lesssim E_\gamma \lesssim$ 100 TeV; VHE). Such variability has been observed in several BL Lac objects (e.g., [Gaidos et al. 1996](#); [Aharonian et al. 2007](#); [Albert et al. 2007b](#); [Aleksić et al. 2011](#)), including the prototypical BL Lacertae (VER J2202+422; [Arlen et al. 2013](#)), located at a redshift of $z = 0.069$ ([Miller & Hawley 1977](#)). Long-term monitoring of BL Lacertae has led to no detection of the source in the TeV gamma-ray band by the current generation of instruments except during flaring episodes, when its flux has been observed to reach >100% of the Crab Nebula flux (C. U.) above 1 TeV in 1998 ([Neshpor et al. 2001](#)), ~ 0.03 C. U. above 200 GeV in 2005 ([Albert et al. 2007a](#)), and most recently ~ 1.25 C. U. above 200 GeV with a short variability timescale of 13 ± 4 min in 2011 ([Arlen et al. 2013](#)).

The rapid gamma-ray variability observed from TeV blazars implies very compact emitting regions, as well as low gamma-ray attenuation from pair production on infrared/optical photons near the emission zone. In a one-zone synchrotron self-Compton model, the intrinsic pair-production opacity of a relativistic emission zone depends on its size and Doppler factor, and on the density of lower-energy photons. Therefore, if the synchrotron photons are the main source of the lower-energy radiation, the emitting region must have a small size and/or a large Doppler factor so that the gamma rays can

escape pair production. Alternatively, if an external photon field (e.g., the broad-line region; BLR) dominates the lower-energy radiation, it can cause substantial gamma-ray absorption. As a result, the emitting region is generally expected to be far away from the central region of the AGN, especially for flat-spectrum radio quasars whose broad-line emission is relatively strong.

The large Doppler factor and/or distant downstream emitting region required by the observed fast TeV variability, together with the knotty jet structures (both moving and stationary) identified with high-resolution radio observations, can be explained consistently by theoretical models with multiple emitting zones that are either spatially or temporally separated, e.g., structured jets ([Ghisellini et al. 2005](#)), jet deceleration ([Stern & Poutanen 2008](#)), jets in a jet ([Giannios et al. 2009](#)), and plasma passing a standing shock (e.g., [Marscher 2014](#); [Zhang et al. 2014](#); [Hervet et al. 2016](#); [Pollack et al. 2016](#)).

However, the details regarding the location and the mechanism of blazar emission are still not well understood. Simultaneous multiwavelength (MWL) observations can provide insights into the flaring mechanisms (e.g., leptonic or hadronic processes) of these objects, particularly at the wavelengths where the spectral energy distributions (SEDs) often peak. In practice, such observations are challenging in the case of fast flares at sub-hour timescales, even with dedicated strategies (e.g., [Abeysekara et al. 2017](#)). Nevertheless, contemporaneous radio data are often relevant because the radio variability timescale is usually much longer. In particular, the evolution of polarization (both radio and optical) before and after a gamma-ray flare provides information about magnetic field structures of the jet, and therefore the activity of possible gamma-ray emitting regions (e.g., [Zhang et al. 2014](#)).

BL Lacertae exhibits both stationary radio cores/knots and superluminal radio knots (Lister et al. 2013; Gómez et al. 2016). Possible associations between the variability of superluminal radio knots and gamma-ray flares have been investigated for BL Lacertae (e.g., Marscher et al. 2008; Arlen et al. 2013) and other blazars (e.g., Rani et al. 2014; Max-Moerbeck et al. 2014).

On 2016 Oct 5, the Very Energetic Radiation Imaging Telescope Array System (VERITAS) observed BL Lacertae at an elevated flux level (see Section 2.1). A series of observations with the Very Long Baseline Array (VLBA) were taken at 43 GHz and 15.4 GHz over the span of a few months before and after the gamma-ray flare, revealing a possible knot structure emerging around the time of the TeV flare (see Section 2.5). In this work, we report on the results of the VERITAS, VLBA, and other MWL observations and discuss their implications. The cosmological parameters assumed throughout this paper are $\Omega_m = 0.27$, $\Omega_\Lambda = 0.73$, and $H_0 = 70 \text{ km s}^{-1} \text{ Mpc}^{-1}$ (Larson et al. 2011). At the redshift of BL Lacertae, the luminosity distance and the angular size distance are 311 Mpc and 273 Mpc, respectively, and the angular scale is 1.3 pc/mas.

2. OBSERVATIONS, DATA ANALYSIS, AND RESULTS

2.1. VERITAS

VERITAS is an array of four imaging atmospheric-Cherenkov telescopes located in southern Arizona (30° 40' N, 110° 57' W, 1.3 km above sea level; Holder 2011). It is sensitive to gamma rays in the energy range from 85 GeV to >30 TeV with an energy resolution of $\sim 15\%$ (at 1 TeV) and is capable of making a detection at a statistical significance of 5 standard deviations (5σ) of a point source of 0.01 C. U. in ~ 25 hr.

BL Lacertae was observed at an elevated TeV gamma-ray flux by VERITAS on 2016 Oct 5 as part of an ongoing monitoring program, and follow-up observations were immediately instigated based on a real-time analysis. The total exposure of these observations amounts to 153.5 min after data-quality selection, with zenith angles ranging between 11° and 30°. The data were analyzed using two independent analysis packages (Cogan 2008; Daniel 2008) and a pre-determined set of cuts optimized for lower-energy showers (see e.g., Archambault et al. 2014). A detection with a statistical significance of 71σ was made from the data on the night of the flare, with a time-averaged integral flux above 200 GeV of $(2.24 \pm 0.06) \times 10^{-6} \text{ photon m}^{-2} \text{ s}^{-1}$ (or ~ 0.95 C. U.).

2.1.1. VHE gamma-ray flux variability and the modelling of the flare profile

Figure 1 shows the VERITAS TeV gamma-ray light curve of BL Lacertae above 200 GeV on 2016 Oct 5 with 4-minute and 30-minute bins. A gradual rise of the TeV flux by a factor of ~ 2 followed by a faster decay was observed. The measured peak flux for the 30-minute-binned light curve is $(3.0 \pm 0.2) \times 10^{-6} \text{ photon m}^{-2} \text{ s}^{-1}$, corresponding to ~ 1.25 C. U., and that for the 4-minute-binned light curve is $(4.2 \pm 0.6) \times 10^{-6} \text{ photon m}^{-2} \text{ s}^{-1}$, or ~ 1.8 C. U.

We first fitted the 4-minute-binned VERITAS light curve with a constant-flux model, obtaining a χ^2 value of 170.8 for 45 degrees of freedom (DOF), corresponding to a p -value of 1.1×10^{-16} and rejecting the constant-flux hypothesis.

To quantify the rise and decay times of the TeV flare, we then fitted the VHE gamma-ray light curve with a piecewise exponential function as follows:

$$F(t) = \begin{cases} F_0 e^{(t-t_{\text{peak}})/t_{\text{rise}}}, & t \leq t_{\text{peak}}; \\ F_0 e^{-(t-t_{\text{peak}})/t_{\text{decay}}}, & t > t_{\text{peak}}; \end{cases} \quad (1)$$

where F_0 is the peak flux, t_{peak} is the time of the peak flux, and t_{rise} and t_{decay} are the rise

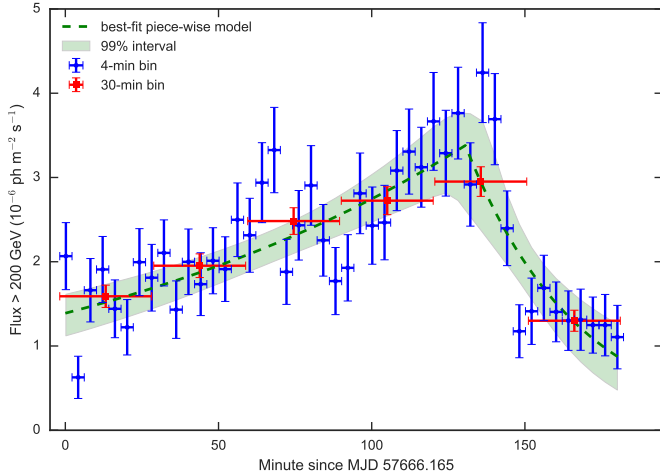


Figure 1. The VERITAS TeV gamma-ray light curves of BL Lacertae above 200 GeV on 2016 Oct 5 (minute zero corresponds to 03:57:36 UTC). The blue dots show the light curve in 4-min bins, and the red squares show the light curve in 30-min bins. The green dashed line and shaded region show the best-fit model (see Equation 1) and its 99% confidence interval, respectively, based on simulations using Markov chain Monte Carlo sampling.

and decay times, respectively, on which the flux varies by a factor of e .

The optimal values of the parameters and their uncertainties were determined from the posterior distributions obtained from Markov chain Monte Carlo (MCMC) simulations, for which the Python package `emcee` (Foreman-Mackey et al. 2013) was used. The MCMC chain contains 100 random walkers in the parameter space initialized with a uniform random prior. Each random walker walks 4000 steps, the first 2000 steps of which are discarded as the “burn-in” samples. This amounts to 2×10^5 effective MCMC simulations. A proposal scale parameter was chosen so that the mean proposal acceptance fraction is 37%, ensuring an adequate yet efficient sampling of the posterior distributions. Note that the parameters are

bounded to be positive, so that they are physically meaningful, and sufficiently large upper bounds were also provided for computational efficiency. After the posterior distributions were obtained, kernel density estimation with Gaussian kernels of bandwidths equal to 1% of the range of the corresponding parameter was used to estimate the most likely value (maximum a posteriori) and the 68% confidence interval of each parameter.

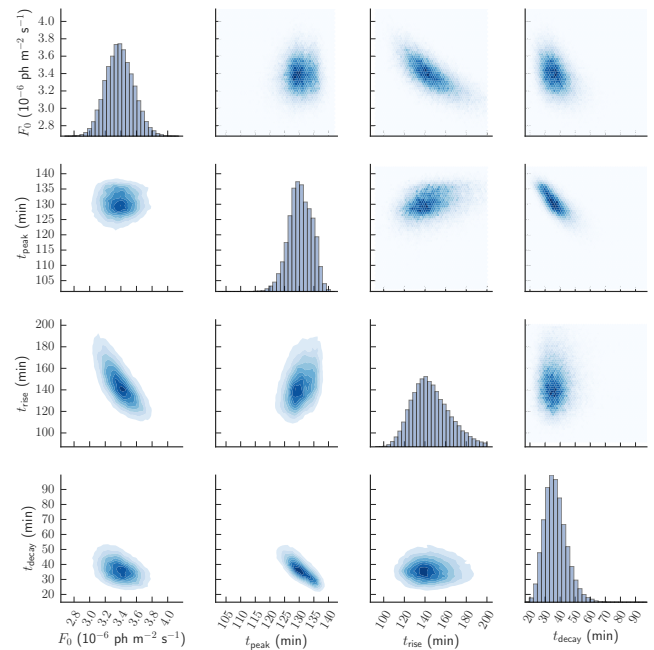


Figure 2. The joint posterior distributions of the parameters in Equation 1 obtained via MCMC simulations. The diagonal plots show the probability distribution histograms of individual parameters; the upper and lower diagonal plots show the two-dimensional histograms with hexagon binning and the kernel density estimations of the joint posterior distributions, respectively.

The joint posterior distributions of the parameters from the MCMC sampling are shown in Figure 2. The diagonal plots show the posterior probability distributions of each parameter, some of which (e.g., t_{peak}) appear non-Gaussian.

Correlations between t_{peak} and t_{rise} , as well as between t_{peak} and t_{decay} , are also apparent in the off-diagonal joint distributions. The best-fit model and the 99% confidence intervals from the MCMC sampling are shown in Figure 1. The rise and decay times of the flare are determined to be 140_{-11}^{+25} min and 36_{-7}^{+8} min, respectively. The best-fit peak time and flux are 130_{-3}^{+5} min (after MJD 57666.165) and $3.4_{-0.2}^{+0.2} \times 10^{-6}$ photon $\text{m}^{-2} \text{s}^{-1}$, respectively.

Further VERITAS observations of BL Lacertae were made on 2016 Oct 6 with 37.6-minute live exposure, and from Oct 22 to Nov 19 with 294.6-minute live exposure, after data-quality selection; neither of these sets of observations led to a detection of the source (signal significances of only 2.6σ and 0.9σ , respectively). The integral flux upper limits (shown in the first panel of Figure 5) between 0.2 and 30 TeV at 99% confidence level from the observations on Oct 6 and between Oct 22 and Nov 19 were obtained as 2.0×10^{-7} photon $\text{m}^{-2} \text{s}^{-1}$ and 2.8×10^{-8} photon $\text{m}^{-2} \text{s}^{-1}$, respectively, assuming a power-law spectrum with a photon index of 3.3 (see Section 2.1.2).

Motivated by the existence of multiple radio emission zones identified in VLBA data (see Section 2.5) and several multi-zone models for BL Lacertae that are consistent with past observations (e.g., Raiteri et al. 2013; Hervet et al. 2016), we also fitted the light curve with a model including a constant-flux baseline. In a multi-zone model, different zones can be of different sizes and vary independently on different timescales. Therefore, it is possible to have a larger emitting zone that varies slowly which can be adequately described by a constant baseline on the timescale considered, and a smaller, more energetic zone that is responsible for the fast flare described by the exponential components. With the more complex model, the best-fit decay time is only $2.6_{-0.8}^{+6.7}$ min, with a baseline flux of $1.2_{-0.2}^{+0.1} \times 10^{-6}$ photon $\text{m}^{-2} \text{s}^{-1}$. The

baseline flux is higher than the upper limit obtained from the observations on the next day, indicating that the slower component would be required to vary on timescales of ~ 1 day, consistent with the GeV observations (Section 2.2). However, we would like to highlight that it is not possible to unambiguously reject either model based on the statistics.

2.1.2. The VHE spectrum

A power-law fit to the VERITAS spectrum of BL Lacertae yields a best-fit photon index of 3.28 and a reduced χ^2 value $\chi^2/\text{DOF} = 30.6$, indicating that a simple power law does not adequately describe the spectrum.

A log-parabola model fits the VERITAS spectrum better:

$$\begin{aligned} \frac{dN}{dE} &= (2.22 \pm 0.07) \times 10^{-5} \\ &\times \left(\frac{E}{0.2 \text{ TeV}} \right)^{[-(2.4 \pm 0.1) - (1.8 \pm 0.3) \log_{10}(\frac{E}{0.2 \text{ TeV}})]} \\ &\text{m}^{-2} \text{s}^{-1} \text{TeV}^{-1}, \end{aligned} \quad (2)$$

with $\chi^2/\text{DOF} = 1.6$.

After de-absorbing the VHE spectrum using the optical depths for a source at a redshift of 0.069 according to the extragalactic background light model in Domínguez et al. (2011), the best-fit log-parabola model becomes:

$$\begin{aligned} \frac{dN}{dE} &= (2.36 \pm 0.07) \times 10^{-5} \\ &\times \left(\frac{E}{0.2 \text{ TeV}} \right)^{[-(2.2 \pm 0.1) - (1.4 \pm 0.3) \log_{10}(\frac{E}{0.2 \text{ TeV}})]} \\ &\text{m}^{-2} \text{s}^{-1} \text{TeV}^{-1}, \end{aligned} \quad (3)$$

with $\chi^2/\text{DOF} = 1.7$. The observed and de-absorbed TeV gamma-ray spectra are shown together with the GeV gamma-ray spectra (Section 2.2) in Figure 3 in the νF_ν representation.

2.2. *Fermi*-LAT

The Large Area Telescope (LAT) on board the *Fermi* satellite is a pair-conversion gamma-ray telescope sensitive to energies from ~ 20 MeV to >300 GeV (Atwood et al. 2009).

An unbinned likelihood analysis was performed with the LAT ScienceTools v10r0p5 and Pass-8 P8R2_SOURCE_V6_v06 instrument response functions (Atwood et al. 2013). SOURCE class events with energy between 100 MeV and 300 GeV within 10° from the position of BL Lacertae were selected. For the short durations of interest to the TeV flare, a simple model containing BL Lacertae, another point source 3FGL J2151.6+4154 $\sim 2^\circ$ away from BL Lacertae, and the contributions from the Galactic (g11_iem_v06) and isotropic (iso_P8R2_SOURCE_V6_v06) diffuse emission were included. We checked in the residual test-statistics map that no significant excess was left unaccounted for within the model. For the short durations, a power law was used to model BL Lacertae instead of the log-parabola model used in the 3FGL catalog.

For the light curve shown in the second panel of Figure 5, an unbinned likelihood analysis was performed on each one-day interval, leaving the normalizations and power-law indices of BL Lacertae and 3FGL J2151.6+4154 free, as well as the normalization of the diffuse components. The source was in an elevated GeV gamma-ray state when the TeV flare was observed, although the GeV flux varied on a much longer timescale. An exponential fit to a 15-day interval around the TeV gamma-ray flare yields a rise time of 2.1 ± 0.2 days and a decay time of 7 ± 2 days.

The gamma-ray SEDs measured by the *Fermi*-LAT and VERITAS on the night of the TeV flare are shown in Figure 3. The best-fit power-law indices of BL Lacertae for the strictly simultaneous and the three-day LAT data are 1.83 ± 0.21 and 1.85 ± 0.07 , respectively. Both

the GeV and TeV gamma-ray spectral indices of this flare in 2016 are comparable to those of the flare in 2011 (Arlen et al. 2013).

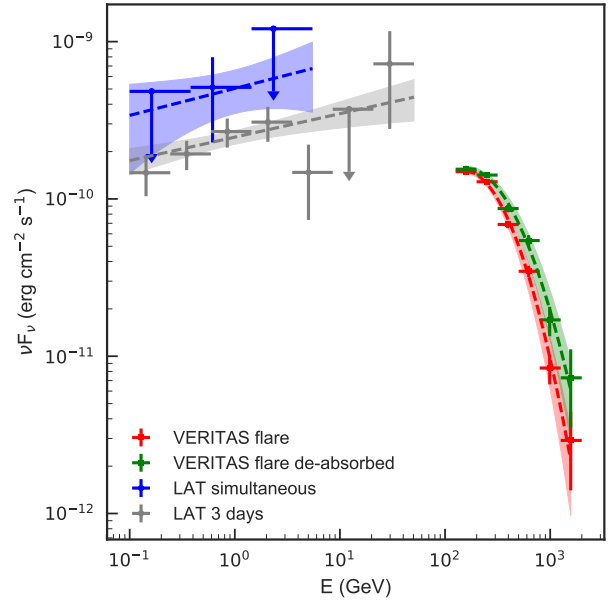


Figure 3. The gamma-ray SEDs of BL Lacertae measured by *Fermi*-LAT and VERITAS. The *Fermi*-LAT SEDs strictly simultaneous with VERITAS observations on 2016 Oct 5 and from the three days around it are shown in blue and grey, respectively. The observed and de-absorbed VERITAS SEDs averaged over all observations on the night of the flare are shown in red and green, respectively. The shaded regions represent $1\text{-}\sigma$ confidence intervals derived from the best-fit spectral models.

2.3. *Swift* XRT

The X-Ray Telescope (XRT) onboard the *Swift* satellite is a grazing-incidence focusing X-ray telescope sensitive to photons in the energy range 0.2–10 keV (Gehrels et al. 2004; Burrows et al. 2005).

Follow-up observations of BL Lacertae were carried out with the *Swift*-XRT on 2016 Oct 6, 7, and 8; the only other XRT observations within a 45-day window around the time of the VHE flare were made on 2016 Oct 27 and Nov 2. The XRT data, taken in the photon-counting

(PC) mode, were analyzed using the `HEASOFT` package (v6.19). The data were first processed using `xrtpipeline` (v0.13.2). The count rates in the PC mode were > 0.5 count s^{-1} , and the effect of potential pile-up was checked for all observations by fitting a King function to the point-spread functions (PSFs) at $>15''$ (Moretti et al. 2005). Those central pixels where the data fall below the model, indicating pile-up, were excluded.

For the observations on 2016 Oct 6, the King function agrees with the data even on the brightest pixels. Therefore, a circular source region of a radius of 20 pixels centered on BL Lacertae was used. For the data taken on 2016 Oct 7 and 8, annular source regions were used, with inner radii of four and two pixels, and an outer radius of 20 pixels. For all three observations, an annular background region with inner and outer radii of 70 and 120 pixels, respectively, was used. Note that source regions excluding the central two and four pixels were also tested for the observations on 2016 Oct 6, and consistent results were obtained. Therefore, we are confident that no bias was introduced by the different exclusion regions used for pile-up correction.

The observations on Oct 7 consisted of two intervals of duration 486 s and 1422 s, separated by roughly one satellite orbital period (~ 90 min). A sustained dark stripe (likely due to bad CCD columns) appears in the XRT image near the position of BL Lacertae, contaminating the second interval. Therefore, we conservatively chose to use only the data recorded during the first interval. The image and spectrum of each ~ 3 min of this relatively short exposure were checked for data quality, and no anomaly was found.

Ancillary response files were generated using the `xrtmkarf` task with the response matrix file `swxpc0to12s6_20130101v014.rmf`. The spectrum was fitted with an absorbed-power-law

Table 1. *Swift*-XRT spectral-fit results using the absorbed-power-law model described in Equation 4, with N_H free and fixed. The errors quoted denote 68% confidence intervals.

Date	α	K	N_H	χ^2/DOF
		$10^{-2} \text{ keV}^{-1} \text{ cm}^{-2} \text{ s}^{-1}$	10^{21} cm^{-2}	
Oct 6	2.5 ± 0.1	$0.62^{+0.07}_{-0.06}$	$2.7^{+0.3}_{-0.3}$	0.83
Oct 7	2.1 ± 0.1	$4.6^{+0.6}_{-0.5}$	$3.1^{+0.5}_{-0.4}$	1.07
Oct 8	2.3 ± 0.1	$0.43^{+0.06}_{-0.05}$	$3.0^{+0.5}_{-0.4}$	0.54
Oct 6	2.54 ± 0.07	0.65 ± 0.03	2.9 (fixed)	0.82
Oct 7	2.08 ± 0.07	4.34 ± 0.24	2.9 (fixed)	1.04
Oct 8	2.26 ± 0.08	0.41 ± 0.02	2.9 (fixed)	0.52

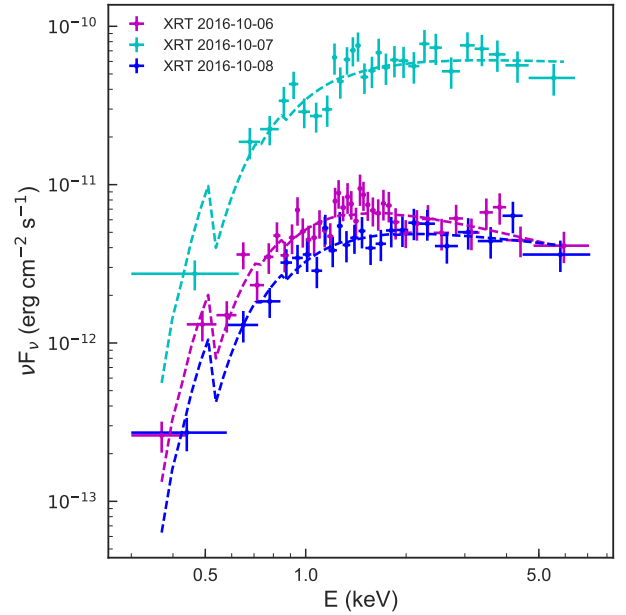


Figure 4. The X-ray SEDs measured by *Swift*-XRT on 2016 Oct 6, 7, and 8. The dashed lines are the best-fit absorbed-power-law model with N_H fixed at $2.9 \times 10^{21} \text{ cm}^{-2}$.

model (`po*wabs`):

$$\frac{dN}{dE} = e^{-N_H \sigma(E)} K \left(\frac{E}{1 \text{ keV}} \right)^{-\alpha}, \quad (4)$$

where N_H is the column density of neutral hydrogen, $\sigma(E)$ is the photoelectric cross-section, and K and α are the normalization and in-

dex of the power-law component, respectively. The best-fit values of the parameters are shown in Table 1. Note that the best-fit values of N_H are in agreement with the archival results from X-ray spectral fit (Madejski et al. 1999; Rivasio et al. 2003; Arlen et al. 2013), but are larger than the value $N_H = 1.8 \times 10^{21} \text{ cm}^{-2}$ from the Leiden/Argentine/Bonn (LAB) survey of Galactic HI (Kalberla et al. 2005). This difference is likely due to the additional contribution of the Galactic molecular gas (e.g., CO emission), as BL Lacertae is relatively close to the Galactic plane (with a Galactic latitude $b = -10.44^\circ$) (Madejski et al. 1999). As the N_H value is expected to stay constant over the period of interest, we also fit the same model with N_H fixed at the average best-fit value $N_H = 2.9 \times 10^{21} \text{ cm}^{-2}$ over the three nights of XRT observations, to better constrain the spectral index and normalization. The X-ray SEDs of BL Lacertae on 2016 Oct 6, 7, and 8 are shown in Figure 4. The X-ray emission from the source was strongest and hardest on 2016 Oct 7 (two days after the TeV gamma-ray flare) compared to the day before and the day after (see Table 1). The energy flux values on 2016 Oct 6, 7, and 8 were (1.4 ± 0.1) , (14.2 ± 0.9) , and $(1.1 \pm 0.1) \times 10^{-11} \text{ erg cm}^{-2} \text{ s}^{-1}$, respectively, as shown in the third panel of Figure 5 along with the results from two more observations taken on 2016 Oct 27 and Nov 2.

2.4. Optical facilities

BL Lacertae was monitored in the R -band at high cadence by a number of optical facilities, including the Steward Observatory¹ (Smith et al. 2009), the AZT-8 reflector of the Crimean Astrophysical Observatory, the Perkins telescope², the LX-200 telescope in St. Petersburg, Russia, and the Calar Alto

2.2-m Telescope (with observations obtained through the MAPCAT³ program) in Almería, Spain. We also included the r' -band observations made with the 48-inch telescope at the Fred Lawrence Whipple Observatory (FLWO). We transformed the r' -band flux to R -band using the color index $V - R = 0.73 \pm 0.19$ for BL Lacertae (Fan et al. 1998) and the transformation $r' - R = 0.19(V - R) + 0.13$ (Smith et al. 2002). The dominant uncertainty from the conversion to R -band comes from the variability of the $V - R$ color index, resulting in an additional systematic uncertainty of ~ 0.04 magnitude, which is included in the converted FLWO R -band magnitude shown in Figure 5. Any variability in the color index $\Delta(V - R) < 0.19$ during the epoch of observations shown would lead to a shift of the FLWO R -band magnitude within the error bars shown.

The R -band flux and polarization measurements around the time of the VHE gamma-ray flare are shown in Figure 5. The lower three panels (from top to bottom) show the R -band magnitude, polarization fraction, and electric vector position angle (EVPA), respectively. A -180° shift is applied to all the EVPA measurements before MJD 57662, so that the EVPA difference between MJD 57662 and 57658 is reduced to $\sim 80^\circ$ from $\sim 100^\circ$ before the shift was applied (see e.g., Abdo et al. 2010). The measurements are reasonably consistent between the various instruments.

The R -band flux from the source varied in a similar manner to the GeV flux, with an increase observed a few days before the VHE flare. The optical EVPA appeared to have rotated smoothly from roughly perpendicular to the position angle (PA) of the jet in late 2016 Sept to roughly parallel in late 2016 Oct, ex-

¹ <http://james.as.arizona.edu/~psmith/Fermi>

² <http://www.lowell.edu/research/research-facilities/1-8-meter-perkins/>

³ MAPCAT stands for the Monitoring of AGN with Polarimetry at the Calar Alto Telescopes, see: http://www.iaa.es/~iagudo/_iagudo/MAPCAT.html

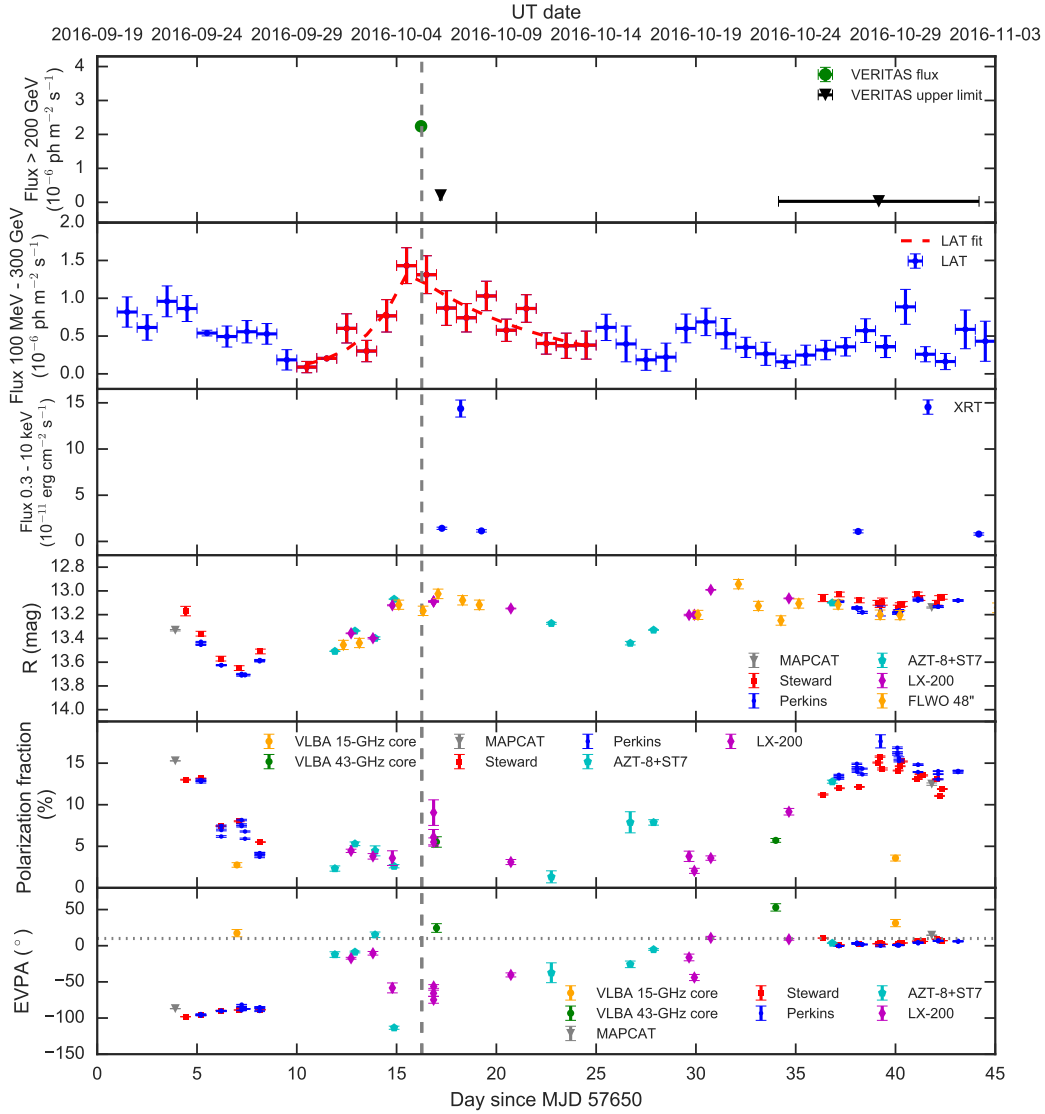


Figure 5. The 45-day MWL light curves of BL Lacertae around the time of the VHE flare. The top panel shows the TeV gamma-ray flux measured by VERITAS on the night of the flare, as well as the upper limits obtained later. The second panel shows the daily-binned GeV gamma-ray light curve measured by *Fermi*-LAT, as well as a piecewise exponential fit (see Equation 1) to a 15-day interval around the TeV gamma-ray flare (red dashed line). The third panel shows the daily-binned X-ray light curve measured by *Swift*-XRT. The lower three panels show the R -band photometric and polarimetric measurements taken by four instruments. The grey vertical dashed line shows the peak time of the TeV flare observed by VERITAS. The fractional polarizations and the EVPAs of the 43-GHz and 15-GHz core are also shown in the bottom two panels. The grey horizontal dotted line in the bottom panel shows the position angle of the jet.

cept for three days before the TeV gamma-ray flare when the optical EVPA was nearly aligned

with the PA of the jet. This was followed by a sudden decrease in EVPA on the day before the

TeV gamma-ray flare. The fractional polarization was relatively low around the time of the TeV flare, and increased to the highest value of the 45-day period in late Oct when the EVPA was again aligned with the jet.

2.5. Radio facilities

BL Lacertae was observed throughout the period of interest at 43 GHz with the Very Long Baseline Array under the VLBA-BU-BLAZAR monitoring program (Jorstad & Marscher 2016) and at 15.4 GHz with the Monitoring Of Jets in Active galactic nuclei with VLBA Experiments (MOJAVE) program (Lister et al. 2009). The 43-GHz and 15.4-GHz VLBA data calibration and imaging procedures were identical to those described by Jorstad et al. (2005) and Lister et al. (2009), respectively.

Figure 6 presents images of the parsec-scale jet of BL Lacertae at five epochs from 2016 Sept 5 to Dec 23. The second epoch, 2016 Oct 6, took place only one day after the VHE flare. The images are convolved with a circular Gaussian restoring beam with a full width at half maximum (FWHM) of 0.1 mas, which is similar to the angular resolution of the longest baselines along the (southern) direction of the jet. We note that the Oct 6 observation was plagued by equipment failure at the Mauna Kea and Hancock antennas, at the extremities of the array, although this degraded the north-south angular resolution by only 14%. The corresponding linear resolution at the redshift of BL Lacertae is 0.13 pc in projection on the sky and $1.8_{-0.4}^{+0.8}$ pc for a viewing angle of $4.2^\circ \pm 1.3^\circ$ between the jet axis and line of sight (Jorstad et al. 2017).

As was the case in earlier observations (Jorstad et al. 2005; Arlen et al. 2013; Gómez et al. 2016; Wehrle et al. 2016), the main structure of the compact jet consists of three quasi-stationary brightness peaks, designated as (from north to south) A0 (used as the positional reference point), A1 0.12 mas to the south, and A2 0.30 mas to the south. The

locations of A1 and A2 appear to fluctuate as moving emission features with superluminal apparent velocities pass through the region. This combination of moving and stationary emission components complicates possible interpretation of the changing structures of the total and polarized intensities. Because of this, the interpretation that we offer to explain the variations within the images is not unique.

We ignore the effects of Faraday rotation on the polarization EVPA, which Jorstad et al. (2007) estimated to be low (-16°) between 43 GHz and 300 GHz. It is worth mentioning that Hovatta et al. (2012) measured a much lower (by an order of magnitude) Faraday rotation using 8-GHz to 15-GHz observations. This could be due to a combination of a possible variability in the rotation measure and a decrease of the rotation measure with distance from the central black hole (Jorstad et al. 2007), as the core at 15 GHz is located further away from the black hole compared to the core at 43 GHz due to the effect of opacity.

A knot of emission with enhanced polarization, which we designate as K16, appears to propagate down the jet. It moves by 0.23 mas between Oct 23, when its centroid is ~ 0.05 mas south of A0, and Dec 23, when it is 0.28 mas from A0. This corresponds to an apparent speed of $6c$, within the range typically observed in BL Lacertae (Jorstad et al. 2005; Marscher et al. 2008; Arlen et al. 2013; Lister et al. 2013; Wehrle et al. 2016; Jorstad et al. 2017). Extrapolation back to Oct 6 places the knot 0.01 mas north of the centroid of A0, within the A0 emission region given A0’s angular size of 0.03 ± 0.02 mas (Jorstad et al. 2017). This interpretation implies that the VHE flare occurred as the knot crossed the “core”, which Marscher et al. (2008) have interpreted as a standing shock located ~ 1 pc from the black hole.

The VLBA images at 15.4 GHz reveal the evolution of the jet structures further away from

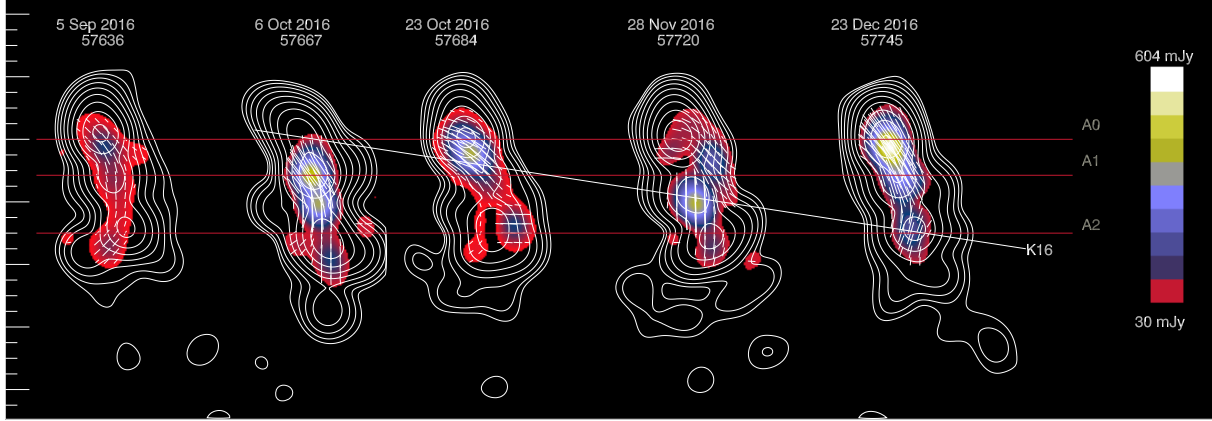


Figure 6. Total (contours) and linearly polarized (color code) intensity images of BL Lacertae from VLBA observations at 43 GHz. The images are convolved with a circular Gaussian restoring beam of FWHM = 0.1 mas. Tick marks are separated by 0.05 mas. The contours are in multiples of $\sqrt{2}$ times the peak of 1.15 Jy/beam. Red horizontal lines indicate the mean locations of the three quasi-stationary components, while the white line shows the motion of moving knot *K16*.

the central source and on a larger spatial scale, as a result of optical depth and angular resolution, respectively, compared with the observations at 43 GHz. Therefore, a delay is expected between the measurements at these two frequencies. Figure 7 shows that the polarized intensity of the stationary core of BL Lacertae at 15.4 GHz reached a minimum on 2016 Dec 26 and gradually increased, with a potential bright feature with distinct polarization angle (consistent with the EVPAs measured at 43 GHz on 2016 Dec 23) on 2016 Dec 10 and 26, which may correspond to the knot *K16* observed at 43 GHz earlier, appearing at ~ 1 mas southwest of the core. This is consistent with past observations of the same source with the VLBA at different frequencies reported by Bach et al. (2006), where new components of the jet were seen to fade as they separated from the core, disappearing at ~ 0.7 mas and reappearing at ~ 1 mas.

We show the fractional polarizations and EVPAs of the 43-GHz and 15-GHz core in the bottom two panels of Figure 5, along with the *R*-band results. The EVPAs of the core at 43 GHz

and 15 GHz are roughly consistent with the PA of 10° of the jet over the course of a few months since 2016 Sept. This implies that the magnetic field is toroidal/helical at the core, as we discuss in Section 3. Further downstream in the jet, the EVPAs become more perpendicular to the PA of the jet, as shown in Figure 7. Such location-dependent radio EVPAs help us to interpret the dominant optical component based on the optical EVPA data.

We show in Figure 8 the evolution of the total flux density of BL Lacertae, measured by the Metsähovi Radio Observatory (MRO) at 37 GHz and by Owens Valley Radio Observatory (OVRO) at 15 GHz, respectively, over about a year, as well as their z-transformed discrete cross-correlation (ZDCF; Alexander 2013).

The 37-GHz observations were made with the 13.7-m diameter Aalto University Metsähovi radio telescope, which is a radome-enclosed Cassegrain-type antenna situated in Finland. The measurements were made with a 1-GHz-bandwidth dual-beam receiver centered at 36.8

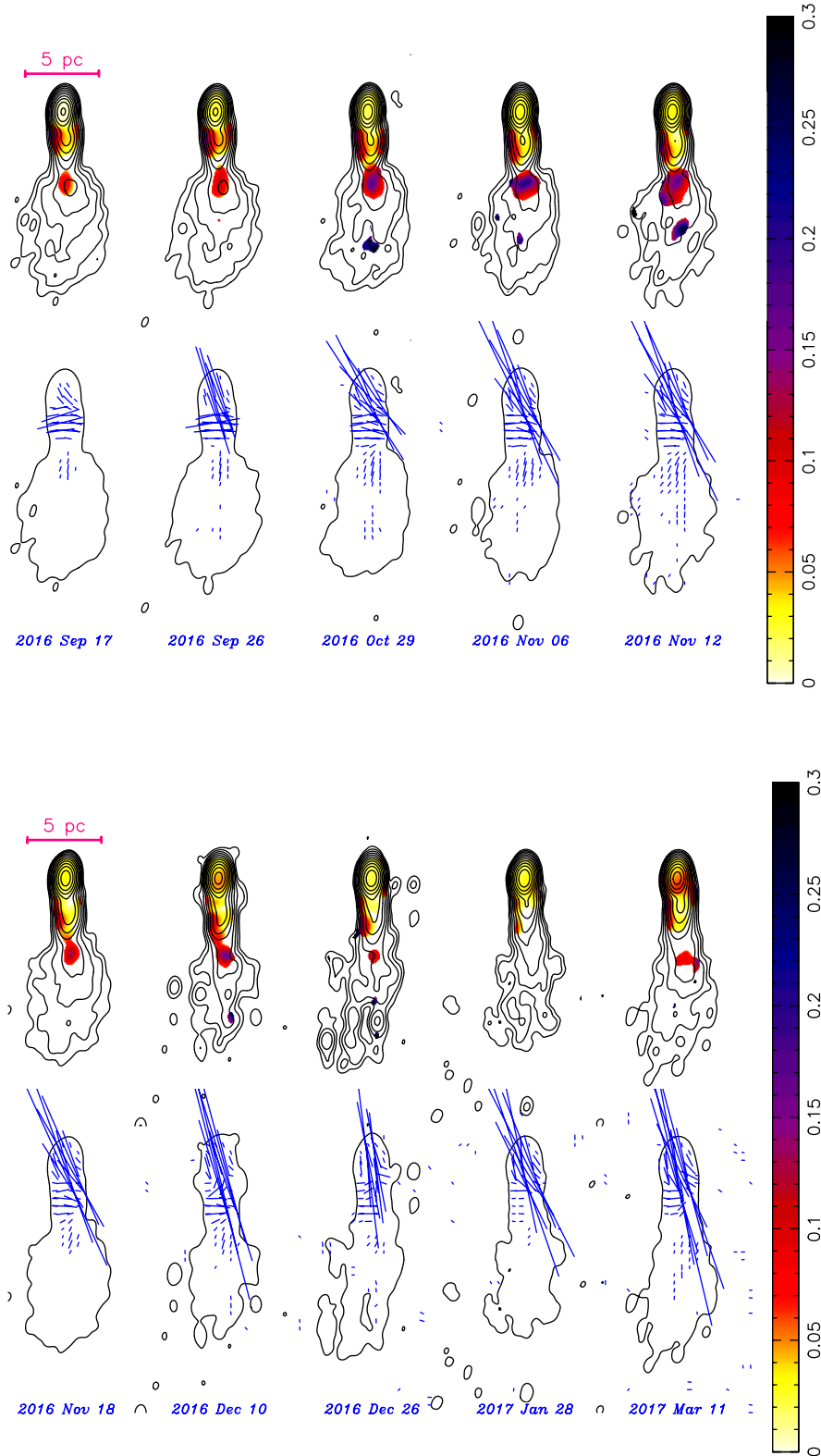


Figure 7. Images of BL Lacertae from VLBA observations at 15.4 GHz for ten epochs. A Gaussian restoring beam with dimensions $0.883 \text{ mas} \times 0.56 \text{ mas}$ and a position angle -8.2° was used. The colors in the top rows of each panel show the fractional polarized level, and the blue line segments in the bottom rows show the EVPA. The contours show the total intensity, with a base contour of 1.1 mJy/beam in both top and bottom rows, and successive contours increment by factors of two in the top rows. The length of the EVPA line segments corresponds to polarized intensity, the lowest of which shown is 0.5 mJy/beam . The typical total and polarized intensity image rms values are 0.09 mJy/beam and 0.1 mJy/beam , respectively.

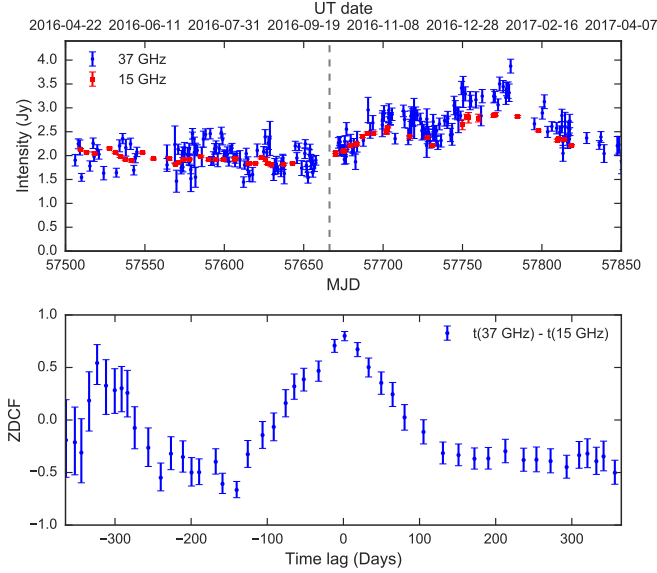


Figure 8. The top panel shows the 37-GHz (blue dots) and 15-GHz (red squares) radio light curves measured over ~ 1 yr by Metsähovi and OVRO, respectively. The grey dashed line shows the peak time of the TeV flare observed by VERITAS. The bottom panel shows the z -transformed discrete cross correlation between the two light curves above. Positive time lags correspond to the 37-GHz flux leading the 15-GHz flux. No time lags or leads are observed.

GHz. The HEMPT (high electron mobility pseudomorphic transistor) front end operates at room temperature. The 37-GHz observations are Dicke-switched ON–ON observations, alternating the source and the sky in each feed horn to remove atmospheric and ground contamination. Typical integration time to obtain one flux-density data point is between 1200 s and 1600 s. The detection limit of the telescope at 37 GHz is on the order of 0.2 Jy under optimal conditions. Data points with a signal-to-noise ratio < 4 are handled as non-detections.

The flux-density scale is set by observations of the HII region of DR 21. Sources NGC 7027, 3C 274 and 3C 84 are used as secondary calibrators. A detailed description of the data reduction and

analysis is given in Teräsranata et al. (1998). The error estimate in the flux density includes the contributions from the measurement rms and the uncertainty of the absolute calibration.

The OVRO 40-m telescope uses off-axis dual-beam optics and a cryogenic pseudo-correlation receiver with a 15.0-GHz center frequency and 3-GHz bandwidth. The source is alternated between the two beams in an ON–ON fashion to remove atmospheric and ground contamination. The fast gain variations are corrected using a 180° phase switch. Calibration is achieved using a temperature-stable diode noise source to remove receiver gain drifts, and the flux-density scale is derived from observations of 3C 286 assuming the Baars et al. (1977) value of 3.44 Jy at 15.0 GHz. The systematic uncertainty of about 5% in the flux density scale is not included in the error bars in Figure 8. Complete details of the reduction and calibration procedures are given in Richards et al. (2011).

The 37-GHz and 15-GHz light curves show that at the time of the TeV gamma-ray flare, BL Lacertae was transitioning from a steady radio flux state to a flaring state that lasted for about five months. The ZDCF shows no significant detection of any time lag between the fluxes at the two frequencies, suggesting that both observations are dominated by the flux from a region that is optically thin at 15 GHz.

3. DISCUSSION

For the second time by VERITAS, a fast gamma-ray flare from BL Lacertae has been observed. While no information was obtained from the rising phase of the first VHE flare in 2011 (Arlen et al. 2013), the VERITAS measurements during the 2016 flare described in this work cover both the rise and decay phases of the flare.

The fastest timescale of a flare (in this case the decay time) can be used to place an upper

limit on the size R of the emitting region, as

$$R \leq \frac{ct_{\text{decay}}\delta}{1+z}, \quad (5)$$

where c is the speed of light, z is the redshift of the source, and δ is the Doppler factor of the jet⁴.

The mass of the central black hole (M_{BH}) of BL Lacertae was estimated to be $\sim 3.8 \times 10^8 M_{\odot}$ by Wu et al. (2009) using the R -band absolute magnitude and the empirical correlation between black hole mass and bulge luminosity of the host galaxy (McLure & Dunlop 2002). The corresponding Schwarzschild radius R_s of the central black hole of BL Lacertae is $\sim 1.1 \times 10^{12}$ m ($\sim 3.6 \times 10^{-5}$ pc). It is worth noting that the mass measurement of a black hole is a challenging task, and M_{BH} values in the range $(0.16 - 5.01) \times 10^8 M_{\odot}$ have been reported for BL Lacertae (see Gupta et al. 2012, and references therein).

The Doppler factor δ was estimated to be ~ 24 according to the method described in Hervet et al. (2016) from the propagation of a possible perturbation in the radio jet observed with VLBA at 15 GHz (Lister et al. 2013), assuming a viewing angle of 2.2° based on radio apparent-velocity measurements. Taking the best-fit value of $t_{\text{decay}} = 36_{-7}^{+8}$ min (see Section 2.1.1), the upper limit of the size of the emitting region can be estimated using Equation 5 to be $R \lesssim 11.9 R_s$.

An asymmetric profile with a faster decay of the VHE gamma-ray flux was observed in the flare, which would be caused by an abrupt cessation of the high-energy particle injection (see e.g., Katarzyński et al. 2003). In this scenario, the flaring activity is attributed to fresh injection of high-energy particles into the emitting region instead of *in situ* acceleration of the par-

ticles. However, minimal variability in the radio band would be observable for this interpretation. The asymmetric flare is in contrast to the more frequently observed flaring profile, a fast rise followed by a slow decay, which can be the manifestation of *in situ* acceleration and/or a longer cooling time (i.e., longer than the acceleration time) associated with a steep particle-energy distribution (analogous to solar flares; see e.g. Harra et al. 2016).

BL Lacertae showed an enhancement in its GeV gamma-ray flux at the time of the TeV flare, but on a longer timescale of a few days. It also exhibited high X-ray flux on 2016 Oct 7 (two days after the TeV flare), about a factor of 10 stronger than the flux on Oct 6 and 8. These observations indicate efficient acceleration of relativistic particles in the jet to at least a few hundred GeV.

Without simultaneous MWL observations of similar temporal resolution, we constrain the Lorentz factor (Γ) and the distance (r) from the central black hole of the gamma-ray-emitting region following the method described by Nalewajko et al. (2014). The collimation constraint was derived from the requirement $\Gamma\theta \lesssim 1$. Both synchrotron self-Compton (SSC) and external-radiation Compton (ERC) processes are considered in the calculation of the SSC constraint, while the majority of the gamma rays are assumed to be produced via ERC process. For the cooling constraint, only the ERC process on the thermal radiation fields close to the black hole is considered. This does not take into account any possible inverse-Compton scattering of an external synchrotron field, which, as we consider below, would loosen the cooling constraint on Γ at large distances from the central black hole. We also assume that the emitting region is spherically symmetric. It is possible that the emitting region is not spherical (e.g., if it is passing a standing shock), and the constraints on Γ and r may change.

⁴ $\delta = [\Gamma(1 - \beta \cos\theta)]^{-1}$, where Γ is the bulk Lorentz factor of the jet, and θ is the angle between the axis of the jet and the line of sight.

Table 2. The parameters used to calculate the constraints shown in Figure 9.

L_{gamma}	L_{syn}	L_{d}^{a}	t_{var}	M_{BH}^{b}	E_{cool}	δ/Γ	ϵ_{BLR}	ϵ_{IR}	r_{BLR}	r_{IR}	E_{BLR}	E_{IR}	g_{SSC}	g_{ERC}
(erg s^{-1})	(erg s^{-1})	(erg s^{-1})	(min)	(M_{\odot})	(TeV)				(pc)	(pc)	(eV)	(eV)		
7.8×10^{45}	7.8×10^{44}	6.0×10^{44}	36	3.8×10^8	1	1	0.1	0.1	0.025	0.5	10	0.3	0.75	0.5

NOTE— L_{gamma} , L_{syn} , and L_{d} are the observed gamma-ray luminosity, the synchrotron luminosity, and disk luminosity, respectively; t_{var} is the observed variability time; M_{BH} is the mass of the central black hole; E_{cool} is the energy of the observed photons due to the external Compton cooling of relativistic electrons; δ/Γ is the ratio between the Doppler factor and Lorentz factor of the electrons; ϵ_{BLR} , r_{BLR} , and E_{BLR} are the covering factor, characteristic radius of the BLR, and the energy of BLR photons, respectively; ϵ_{IR} , r_{IR} , and E_{IR} are similar parameters for the IR-emitting torus region; g_{SSC} and g_{ERC} are the bolometric correction factors for SSC and ERC mechanisms.

^aAbdo et al. (2011)

^bWu et al. (2009)

The values of the parameters used for the calculation of the above three constraints on Γ and r are shown in Table 2. Some of the parameters are constrained by observations, and the other parameters are chosen so that a conservative constraint is derived. For example, we set the Compton dominance parameter $q = L_{\text{gamma}}/L_{\text{syn}} = 10$ based on the observed R -band magnitude and the peak flux of the gamma-ray SED, the former of which should provide a good estimation of the peak of the synchrotron flux, considering that the source is a lower-frequency-peaked BL Lac object. The SSC luminosity was set equal to the observed gamma-ray luminosity $L_{\text{SSC}} = L_{\text{gamma}}$ in order to obtain a conservative SSC constraint. We also used a relatively-high observed gamma-ray energy (1 TeV) for a conservative ERC cooling limit. We note that changes in the values of the parameters describing the geometry of the external radiation fields, namely the covering factor ϵ_{BLR} and characteristic radius r_{BLR} for the BLR, and similarly ϵ_{IR} and r_{IR} for the IR torus, which are poorly constrained by observations, could change the cooling constraint. The values of the radii used in this work are derived based on the disk luminosity $L_{\text{d}} = 6.0 \times 10^{44} \text{ erg s}^{-1}$ (Abdo et al. 2011) and the relations $r_{\text{BLR}} = 1 \times 10^{15} \sqrt{(L_{\text{d}}/10^{45} \text{ erg s}^{-1})} \text{ m} \approx 0.025 \text{ pc}$ and $r_{\text{IR}} = 2 \times 10^{16} \sqrt{(L_{\text{d}}/10^{45} \text{ erg s}^{-1})} \text{ m} \approx 0.5 \text{ pc}$ (Ghisellini & Tavecchio 2015).

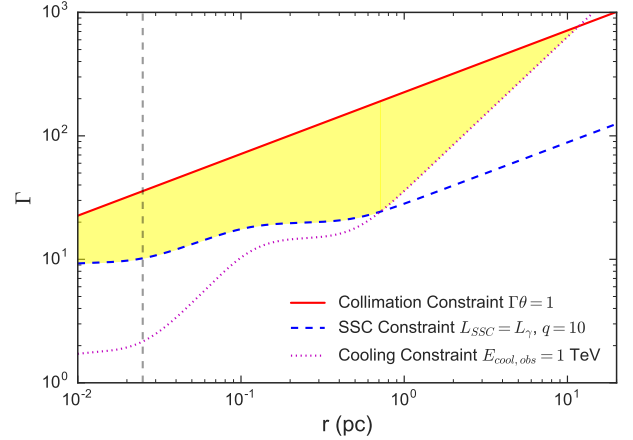


Figure 9. The constraints on the Lorentz factor (Γ) and the distance (r) between the central black hole and the gamma-ray emitting location. The gray vertical dashed line indicates the location of the BLR (0.025 pc) used in the calculation. The yellow shaded region illustrates the allowed parameter space.

In this analysis, the distance r between the central black hole and the gamma-ray-emitting region is constrained to be $\lesssim 12.4 \text{ pc}$. If we fix the Lorentz factor at $\Gamma = 24$, then we constrain the distance to be $0.01 \lesssim r/\text{pc} \lesssim 0.7$. If we fix the distance at $r = 1 \text{ pc}$, the estimated distance between the core $A0$ and the central black hole, and assume that the gamma rays are produced as the knot $K16$ passes the core $A0$, then

the Lorentz factor is only loosely constrained at $35 \lesssim \Gamma \lesssim 226$.

At small r values ($r \lesssim 0.68$ pc), the SSC constraint on the lower limit of Γ is stricter than the cooling constraint. At $r = r_{\text{BLR}} = 0.025$ pc (the smallest distance for the VHE-emitting region without heavy absorption from the radiation field in the BLR), we put a strong lower limit on the Lorentz factor $\Gamma \gtrsim 10.1$, which is larger than the archival values ($\sim 5\text{--}7$) derived from radio observations (Jorstad et al. 2005, 2017), and consistent with the value of 24 adopted in this work. A possible explanation for the lower values of Γ obtained from the radio observations is that they are calculated based on the apparent velocity of the superluminal features in the jet, which may travel at a lower speed compared to the bulk plasma flow (e.g., Lister et al. 2013; Hervet et al. 2016).

At large r values ($r \gtrsim 2$ pc), the lower limit on the Lorentz factor Γ increases to > 100 , exceeding the typical range of $\Gamma \sim 4\text{--}50$ obtained from observations of blazars (e.g., Jorstad et al. 2005; Cohen et al. 2007; Lister et al. 2016). This indicates that another seed-photon population, such as an external synchrotron radiation field, is needed if the gamma-ray-emitting region lies beyond ~ 2 pc.

The 43-GHz and 15-GHz observations reveal that the EVPAs at the core are mostly parallel to the PA of the jet. This implies that the magnetic field is likely toroidal or strongly helical near the core, consistent with earlier observations of BL Lacertae (e.g., Gómez et al. 2016). The 15-GHz EVPAs at larger distances away from the core become more perpendicular to the PA of the jet, indicating that the magnetic field likely becomes more poloidal in the outer jet. Such a magnetic field configuration has been proposed for low-frequency-peaked BL Lac objects (e.g., Kharb et al. 2008; Hervet et al. 2016).

Based on these radio observations, we can use the observed changes in the optical polarizations of BL Lacertae (as shown in Figure 5) to gain insights into the magnetic field structure and the location of the region that dominates the optical emission (e.g., D’arcangelo et al. 2009; Algaba et al. 2011). The optical EVPAs were observed roughly perpendicular to the PA of the jet in late 2016 Sept, indicating that the magnetic field is close to being aligned with the jet and likely dominated by the region downstream in the jet at that time. Similarly, the optical EVPAs became mostly parallel to the PA of the jet after late Oct, suggesting that the optical emission was then dominated by the core or the inner jet. We also observed the highest optical fractional polarization during this period, suggesting that the magnetic field of the core/inner jet is more ordered.

During the three days preceding the TeV gamma-ray flare, the optical EVPA became (temporarily) nearly aligned with the PA of the jet, but on the day before the TeV gamma-ray flare it suddenly rotated back to a direction consistent with its direction prior to this quasi-alignment. Such abrupt changes in optical polarization associated with flares are found in numerical simulations for blazars and gamma-ray bursts (Zhang et al. 2014; Deng et al. 2016), and can potentially be interpreted as resulting from the helical motion of an emitting component in a toroidal/helical magnetic field before that component reaches the shocked region (e.g., Marscher et al. 2008). However, since the fractional polarization was relatively low during this period, it is also possible that the observed EVPA change was a random fluctuation due to a turbulent magnetic field.

A superluminal radio knot *K16* was observed through a series of VLBA exposures on BL Lacertae at 43 GHz. Extrapolation of the knot position implies that the VHE gamma-ray flare happened as the knot *K16* crossed the quasi-

stationary radio core. This suggests a possible association between the fast VHE gamma-ray flare and the appearance of the superluminal radio knot for the source, similar to that reported by Arlen et al. (2013).

In the model proposed by Marscher (2014), the radio core is a Mach disk at the apex of a conical shock downstream in the jet, with a transverse orientation with respect to the jet axis. When turbulent cells of plasma pass through the conical shock, relativistic electrons can be accelerated to higher energies in those cells where the magnetic field orientation relative to the shock normal is favorable. A fast gamma-ray flare can happen via inverse-Compton scattering as the relativistic plasma approaches the Mach disk at the end of the conical shock, which provides a dense source of synchrotron and SSC seed photons. After the energized plasma passes the Mach disk, a conical rarefaction causes the flow to expand and accelerate, with the bright plasma appearing as a superluminal radio knot.

In some numerical simulations, the polarization fraction drops as the magnetic field direction changes, while the EVPA can rotate owing to random fluctuation of the field or the emergence of a new field component (e.g., Marscher 2014; Zhang et al. 2014). This is consistent with the optical polarization measurements shortly before the VHE gamma-ray flare (see Figure 5), as well as the VLBA images at 15.4 GHz (see Figure 7). The changing superposition of the magnetic fields as the moving knot (*K16*) passes the quasi-stationary knots (*A0*, *A1*, and *A2*) may also explain the change in the positions of *A0*, *A1*, and *A2* between epochs (see Figure 6).

An alternative hypothesis that can explain both the VHE gamma-ray flare and the superluminal radio knot of BL Lacertae is the breakout of a recollimation-shock zone (Hervet et al. 2016). In this model, one or more recollimation shocks, of similar nature to those

in Marscher (2014), can form upstream in the jet where the magnetic energy density is high and appear as stationary radio knots; further downstream in the jet, particle kinetic energy becomes dominant, the magnetic field becomes unstable, and a stationary knot can be carried away by the underlying relativistic flow and become a superluminal knot. In the case of a compact region with large kinetic energy passing the recollimation-shock zone, a multi-component flare could be observed, with one component that varies slowly (i.e., on timescales of hours), thereby giving the appearance of a quasi-constant baseline in an intra-night light curve, as a result of the following sequence of events. First, in this scenario, an increase in the non-thermal emission of the shock region is expected, which leads to a flux increase on the timescale corresponding to the size of the entire shock region (as the baseline component). As the kinetic power of the jet increases at the shock zone, the magnetic field structure is subject to strong tearing instabilities, at which point a magnetic-reconnection event occurs, leading to the observed fast flare. Finally, the shock zone is dragged away by the flow and enters an adiabatic expansion and cooling phase, leading to a decrease in flux and a return to the low state of the source. In the case of the 2016 flare of BL Lacertae, there is no evidence for the disruption or breakout of a stationary knot, although it is possible that the recollimation zone reformed quickly between VLBA epochs and was therefore not sampled by the observations. Therefore, future observations of flares from gamma-ray blazars, with adequate coverage after the flux decreases, can potentially reduce the ambiguity in the interpretation.

VERITAS is supported by grants from the U.S. Department of Energy Office of Science, the U.S. National Science Foundation and the Smithsonian Institution, and by NSERC in

Canada. We acknowledge the excellent work of the technical support staff at the Fred Lawrence Whipple Observatory and at the collaborating institutions in the construction and operation of the instrument.

The VERITAS Collaboration is grateful to Trevor Weekes for his seminal contributions and leadership in the field of VHE gamma-ray astrophysics, which made this study possible.

The research at Boston University was supported in part by NASA *Fermi* Guest Investigator Program grant NNX14AQ58G. The VLBA is an instrument of the Long Baseline Observatory (LBO). The LBO is a facility of the National Science Foundation operated under cooperative agreement by Associated Universities, Inc.

This research has made use of data from the MOJAVE database that is maintained by the MOJAVE team (Lister et al. 2009) and supported by NASA-*Fermi* grant NNX15AU76G. This work made use of the Swinburne University of Technology software correlator (Deller et al. 2011), developed as part of the Australian Major National Research Facilities Programme and operated under licence. YYK and ABP are partly supported by the Russian Foundation for Basic Research (project 17-02-00197), the government of the Russian Federation (agreement 05.Y09.21.0018), and the Alexander von Humboldt Foundation. T.S. was funded by

the Academy of Finland projects 274477 and 284495.

This research has made use of data from the OVRO 40-m monitoring program (Richards et al. 2011) which is supported in part by NASA grants NNX08AW31G, NNX11A043G, and NNX14AQ89G and NSF grants AST-0808050 and AST-1109911.

The monitoring of BL Lacertae and other blazars at the Steward Observatory is supported through NASA *Fermi* Guest Investigator grant NNX15AU81G.

IA acknowledges support by a Ramón y Cajal grant of the Ministerio de Economía y Competitividad (MINECO) of Spain. Acquisition and reduction of the MAPCAT data was supported in part by MINECO through grants AYA2010-14844, AYA2013-40825-P, and AYA2016-80889-P, and by the Regional Government of Andalucía through grant P09-FQM-4784. The MAPCAT observations were carried out at the German-Spanish Calar Alto Observatory, which is jointly operated by the Max-Planck-Institut für Astronomie and the Instituto de Astrofísica de Andalucía-CSIC.

Facilities: VERITAS, *Fermi*(LAT), *Swift*(XRT), SO:Kuiper, Bok, CrAO:1.25m, CAO:2.2m, Perkins, LX-200, FLWO:1.2m, VLBA, Metsähovi Radio Observatory, OVRO:40m

Software: Emcee (Foreman-Mackey et al. 2013), NumPy (van der Walt et al. 2011), Matplotlib (Hunter 2007), SciPy (Jones et al. 2001), Seaborn (Waskom et al. 2014)

REFERENCES

- Abdo, A. A., Ackermann, M., Ajello, M., et al. 2010, *Nature*, 463, 919
 —. 2011, *ApJ*, 730, 101
 Abeysekara, A. U., Archambault, S., Archer, A., et al. 2017, *ApJ*, 834, 2
 Aharonian, F., Akhperjanian, A. G., Bazer-Bachi, A. R., et al. 2007, *ApJL*, 664, L71
 Albert, J., Aliu, E., Anderhub, H., et al. 2007a, *ApJL*, 666, L17
 —. 2007b, *ApJ*, 669, 862
 Aleksić, J., Antonelli, L. A., Antoranz, P., et al. 2011, *ApJL*, 730, L8
 Alexander, T. 2013, ArXiv e-prints, arXiv:1302.1508

- Algaba, J. C., Gabuzda, D. C., & Smith, P. S. 2011, *MNRAS*, 411, 85
- Archambault, S., Aune, T., Behera, B., et al. 2014, *ApJL*, 785, L16
- Arlen, T., Aune, T., Beilicke, M., et al. 2013, *ApJ*, 762, 92
- Atwood, W., Albert, A., Baldini, L., et al. 2013, ArXiv e-prints, arXiv:1303.3514
- Atwood, W. B., Abdo, A. A., Ackermann, M., et al. 2009, *ApJ*, 697, 1071
- Baars, J. W. M., Genzel, R., Pauliny-Toth, I. I. K., & Witzel, A. 1977, *A&A*, 61, 99
- Bach, U., Villata, M., Raiteri, C. M., et al. 2006, *A&A*, 456, 105
- Burrows, D. N., Hill, J. E., Nousek, J. A., et al. 2005, *SSRv*, 120, 165
- Cogan, P. 2008, in International Cosmic Ray Conference, Vol. 3, International Cosmic Ray Conference, 1385–1388
- Cohen, M. H., Lister, M. L., Homan, D. C., et al. 2007, *ApJ*, 658, 232
- Daniel, M. K. 2008, in International Cosmic Ray Conference, Vol. 3, International Cosmic Ray Conference, 1325–1328
- D’arcangelo, F. D., Marscher, A. P., Jorstad, S. G., et al. 2009, *ApJ*, 697, 985
- Deller, A. T., Brisken, W. F., Phillips, C. J., et al. 2011, *PASP*, 123, 275
- Deng, W., Zhang, H., Zhang, B., & Li, H. 2016, *ApJL*, 821, L12
- Domínguez, A., Primack, J. R., Rosario, D. J., et al. 2011, *MNRAS*, 410, 2556
- Fan, J. H., Xie, G. Z., Pecontal, E., Pecontal, A., & Copin, Y. 1998, *ApJ*, 507, 173
- Foreman-Mackey, D., Hogg, D. W., Lang, D., & Goodman, J. 2013, *PASP*, 125, 306
- Gaidos, J. A., Akerlof, C. W., Biller, S., et al. 1996, *Nature*, 383, 319
- Gehrels, N., Chincarini, G., Giommi, P., et al. 2004, *ApJ*, 611, 1005
- Ghisellini, G., & Tavecchio, F. 2015, *MNRAS*, 448, 1060
- Ghisellini, G., Tavecchio, F., & Chiaberge, M. 2005, *A&A*, 432, 401
- Giannios, D., Uzdensky, D. A., & Begelman, M. C. 2009, *MNRAS*, 395, L29
- Gómez, J. L., Lobanov, A. P., Bruni, G., et al. 2016, *ApJ*, 817, 96
- Gupta, S. P., Pandey, U. S., Singh, K., et al. 2012, *NewA*, 17, 8
- Harra, L. K., Schrijver, C. J., Janvier, M., et al. 2016, *SoPh*, 291, 1761
- Hervet, O., Boisson, C., & Sol, H. 2016, *A&A*, 592, A22
- Holder, J. 2011, International Cosmic Ray Conference, 12, 137
- Hovatta, T., Lister, M. L., Aller, M. F., et al. 2012, *AJ*, 144, 105
- Hunter, J. D. 2007, *Computing in Science and Engineering*, 9, 90
- Jones, E., Oliphant, T., Peterson, P., et al. 2001, *SciPy: Open source scientific tools for Python*, [Online; accessed 2017-02-10]
- Jorstad, S., & Marscher, A. 2016, *Galaxies*, 4, 47
- Jorstad, S. G., Marscher, A. P., Lister, M. L., et al. 2005, *AJ*, 130, 1418
- Jorstad, S. G., Marscher, A. P., Stevens, J. A., et al. 2007, *AJ*, 134, 799
- Jorstad, S. G., Marscher, A. P., Morozova, D. A., et al. 2017, *ApJ*, 846, 98
- Kalberla, P. M. W., Burton, W. B., Hartmann, D., et al. 2005, *A&A*, 440, 775
- Katarzyński, K., Sol, H., & Kus, A. 2003, *A&A*, 410, 101
- Kharb, P., Lister, M. L., & Shastri, P. 2008, *International Journal of Modern Physics D*, 17, 1545
- Larson, D., Dunkley, J., Hinshaw, G., et al. 2011, *ApJS*, 192, 16
- Lister, M. L., Aller, H. D., Aller, M. F., et al. 2009, *AJ*, 137, 3718
- Lister, M. L., Aller, M. F., Aller, H. D., et al. 2013, *AJ*, 146, 120
- . 2016, *AJ*, 152, 12
- Madejski, G. M., Sikora, M., Jaffe, T., et al. 1999, *ApJ*, 521, 145
- Marscher, A. P. 2014, *ApJ*, 780, 87
- Marscher, A. P., Jorstad, S. G., D’Arcangelo, F. D., et al. 2008, *Nature*, 452, 966
- Max-Moerbeck, W., Hovatta, T., Richards, J. L., et al. 2014, *MNRAS*, 445, 428
- McLure, R. J., & Dunlop, J. S. 2002, *MNRAS*, 331, 795
- Miller, J. S., & Hawley, S. A. 1977, *ApJL*, 212, L47
- Moretti, A., Campana, S., Mineo, T., et al. 2005, in *Proc. SPIE, Vol. 5898, UV, X-Ray, and Gamma-Ray Space Instrumentation for Astronomy XIV*, ed. O. H. W. Siegmund, 360–368

- Nalewajko, K., Begelman, M. C., & Sikora, M. 2014, *ApJ*, 789, 161
- Neshpor, Y. I., Chalenko, N. N., Stepanian, A. A., et al. 2001, *Astronomy Reports*, 45, 249
- Pollack, M., Pauls, D., & Wiita, P. J. 2016, *ApJ*, 820, 12
- Raiteri, C. M., Villata, M., D’Ammando, F., et al. 2013, *MNRAS*, 436, 1530
- Rani, B., Krichbaum, T. P., Marscher, A. P., et al. 2014, *A&A*, 571, L2
- Ravasio, M., Tagliaferri, G., Ghisellini, G., et al. 2003, *A&A*, 408, 479
- Richards, J. L., Max-Moerbeck, W., Pavlidou, V., et al. 2011, *ApJS*, 194, 29
- Schlickeiser, R. 1996, *SSRv*, 75, 299
- Smith, J. A., Tucker, D. L., Kent, S., et al. 2002, *AJ*, 123, 2121
- Smith, P. S., Montiel, E., Rightley, S., et al. 2009, *ArXiv e-prints*, arXiv:0912.3621
- Stern, B. E., & Poutanen, J. 2008, *MNRAS*, 383, 1695
- Teräsanta, H., Tornikoski, M., Mujunen, A., et al. 1998, *A&AS*, 132, 305
- van der Walt, S., Colbert, S. C., & Varoquaux, G. 2011, *Computing in Science Engineering*, 13, 22
- Waskom, M., Botvinnik, O., Hobson, P., et al. 2014, *seaborn: v0.5.0* (November 2014), , , doi:10.5281/zenodo.12710
- Wehrle, A. E., Grupe, D., Jorstad, S. G., et al. 2016, *ApJ*, 816, 53
- Wu, Z.-Z., Gu, M.-F., & Jiang, D.-R. 2009, *Research in Astronomy and Astrophysics*, 9, 168
- Zhang, H., Chen, X., & Böttcher, M. 2014, *ApJ*, 789, 66